Mechanistic assessments of NO oxidation turnover rates and active site densities on WO_3-promoted CeO_2 catalysts

Masaoki Iwasaki [a],[1], Enrique Iglesia [a],[b],*

[a] Department of Chemical Engineering, University of California, Berkeley, CA 94720, United States
[b] E.O. Lawrence Berkeley National Laboratory, Berkeley, CA 94720, United States

A B S T R A C T

The effects of NO, NO_2 and O_2 pressures on NO oxidation rates and UV-visible spectra are used here to assess the elementary steps and the number and type of redox-active sites involved in NO oxidation on CeO_2 promoted by contact with WO_3 domains. The reversible chemisorption of O_2 on vacancies (*) and the subsequent dissociation of O_2^* assisted by NO to form O^* and NO_2 are the kinetically-relevant steps on surfaces with O^* coverage set by $NO-NO_2$ equilibration. $O_{2p} \rightarrow Ce_{4f}$ ligand-to-metal charge transfer (LMCT) bands probe the rate constants for O_2^* formation and desorption at catalytic conditions; their comparison with those derived from rate data confirms the mechanistic conclusions and the involvement of CeO_2 surfaces promoted by contact with WO_3 domains. These data allow an accurate assessment of the number and type of redox-active sites, thus allowing reactivity comparisons among catalysts based on turnover rates. The number of redox-active sites increased with increasing W surface density (2.1–9.5 W/nm^2), but NO oxidation turnover rates were essentially unchanged. These elementary steps and active structures differ markedly from those that mediate NO oxidation on Pt, PdO, RhO_2 and Co_3O_4 catalysts. Turnover rates are similar on WO_3/CeO_2 and Pt-based catalysts at practical temperatures of diesel exhaust treatment ($\sim$500 K), but WO_3/CeO_2 catalysts exhibit much higher rates based on catalyst mass (>10-fold), thus rendering useful as less costly and more resilient alternatives to noble metals. These findings illustrate a method to probe the number and type of redox-active sites and conceptual insights into the pathways that mediate the chemisorption and activation of O_2 by isolated vacancies and the subsequent dissociation of O=O bonds by assistance from co-reactants.

© 2016 Elsevier Inc. All rights reserved.

1. Introduction

Nitrogen oxides [NO_x (NO and NO_2)] from hydrocarbon combustion exhaust cause photochemical smog, acid rain, and stratospheric ozone depletion [1,2]. NO_x can be converted into dinitrogen (N_2) via reactions with ammonia (NH_3) in the presence of dioxygen (O_2) via selective catalytic reduction (SCR) processes [3]. The presence of equimolar $NO-NO_2$ mixtures leads to faster reactions ("fast SCR" ($NO + NO_2 + 2NH_3 \rightarrow 2N_2 + 3H_2O$)) than in the absence of NO_2 ($2NO + \frac{1}{2}O_2 + 2NH_3 \rightarrow 2N_2 + 3H_2O$) [4]. The prevalence of NO in effluent streams thus requires NO oxidation to NO_2 for the efficient performance of NH_3-NO_x processes. Metals (Pt [5,6]) and their oxides (PdO [7], RhO_2 [8], Co_3O_4 [8,9], MnO_x

[10]) catalyze these reactions at relevant exhaust conditions; their active sites and reaction mechanism are well understood and involve O_2 activation on vacancies present at surfaces nearly saturated with oxygen adatoms as the kinetically-relevant steps [5–8]. These catalysts, however, are also effective in NH_3 oxidation to NO_x, thus degrading the effectiveness of SCR abatement strategies [11,12].

Recently, Cu cations exchanged into small-pore molecular sieves with chabazite (CHA) frameworks (SSZ-13, SAPO-34) have been found to exhibit excellent SCR activity and hydrothermal stability [13–15]. Theory and experiments have suggested that NO oxidation proceeds via (i) molecular O_2 adsorption on Cu dimers to form $Cu-O_2-Cu$ as a side-on peroxide (η^2-O_2), (ii) NO(g) reactions with these species to form $Cu-O-Cu$ and NO_2(g), and (iii) O-atom removal from $Cu-O-Cu$ by NO(g) to form another NO_2 molecule, with step (ii) as the kinetically-relevant step [16].

Tungsten (W) and niobium (Nb) oxides dispersed on ceria (CeO_2) also exhibit high SCR activity, as well as excellent N_2 selectivity and resistance to sulfur dioxide (SO_2), over a broad temper-

ature range (473–723 K) [17–26]. These catalyst systems are based on non-toxic elements and include WO_3-CeO_2 [17–19], WO_3-CeO_2-TiO_2 [20,21], WO_3-CeO_2-ZrO_2 [22,23], Nb_2O_5-CeO_2 [24,25], and Nb_2O_5-WO_3-CeO_2-TiO_2 compositions [26]. The requirement for acid and redox sites, proposed for SCR on V_2O_5-TiO_2 [27], may also account for the promotional effects of WO_3 on CeO_2, via the formation of acid centers in WO_3 domains [19]. SCR reactions are likely to require acid sites, but such sites do not catalyze NO oxidation at relevant SCR conditions (473–723 K), thus preventing the involvement of fast-SCR pathways that require NO_2 molecules [28,29]. The redox properties of CeO_2 lead to low but detectable NO oxidation reactivity; such properties have been implicated in its promotion of the SCR-reactivity of TiO_2 [30]. Hence, NO oxidation reactivity measurements provide an effective probe of the presence and reactivity of redox sites in these catalysts.

Intrapellet physical mixtures of ZrO_2-supported WO_3 (denoted WO_3/ZrO_2), a prototypical acid catalyst, with CeO_2 led to higher SCR rates but did not influence NO oxidation rates [31]. The dispersion of WO_3 domains onto CeO_2 (WO_3/CeO_2), however, increased both SCR and NO oxidation rates over those on pure CeO_2 [31], suggesting that redox-active sites form via atomic contact between WO_3 domains and CeO_2 surfaces. The mechanistic details of NO oxidation and the nature of such sites on these catalysts remain unclear and are the subject of the present study.

Here, we report NO oxidation turnover rates (normalized by the number of redox-active sites) under conditions of strict kinetic control on WO_3/CeO_2 (2.1–9.5 W nm^{-2}) and CeO_2 to assess the identity and kinetic relevance of the elementary steps involved. We provide evidence for the kinetic relevance of steps involving the reversible molecular adsorption of O_2 followed by the irreversible dissociation of the chemisorbed oxygen molecules (O_2^*) assisted by interactions with NO(g). These conclusions are consistent with UV-visible spectra acquired at steady-state and transient conditions, which detected reversible changes in the ligand-to-metal charge transfer (LMCT) band shifts corresponding to O_2^* species. The number and reactivity of such O_2^* species, formed at reduced Ce centers promoted by interactions with WO_3 domain, were determined from these spectroscopic data and used to normalize rates, thus allowing an accurate determination of active site densities by comparing kinetic parameters obtained from NO oxidation rate data and from LMCT spectral features. These data allowed the first rigorous assessment of the number of active sites involved in catalytic turnovers through the analysis of transient spectra to obtain intrinsic rate constants (i.e. per site) for the kinetically-relevant O_2 activation steps. The quantitative interpretation of the effects of W density on the number of active sites provides fundamental and conceptual insights into the type and genesis of the redox-active sites that form by atomic contact between CeO_2 surfaces and WO_3 domains.

2. Experimental methods

2.1. Catalyst preparation and characterization

CeO_2 powders (Rhodia, 150 $m^2 g^{-1}$) were heated to 873 K at 0.08 K s^{-1} in flowing air (0.3 $cm^3 s^{-1} g^{-1}$) and held for 10 h. These CeO_2 powders (75 $m^2 g^{-1}$, BET surface area) were impregnated to incipient wetness using aqueous ammonium metatungstate solutions ((NH_4)$_6$$H_2$$W_{12}$$O_{40}$, Strem Chemicals, 99.9%) containing the desired amount of W, treated in static ambient air at 383 K overnight, and then, treated in flowing dry air (0.8 $cm^3 s^{-1} g^{-1}$) at 823 K (0.08 K s^{-1}) for 3 h. WO_3/CeO_2 samples prepared with 4, 8 and 13 wt% WO_3 gave BET surface areas of 49, 39 and 35 $m^2 g^{-1}$, corresponding to 2.1, 5.3 and 9.5 W-atom nm^{-2} surface densities, respectively. BET surface areas were determined using the single-

point method (Micro Data, Micro Sorp 4232II) after treatment at 523 K for 0.33 h in N_2 flow (0.4 $cm^3 s^{-1}$).

WO_3/ZrO_2 samples were also prepared in a similar manner to WO_3/CeO_2. ZrO_2 powders (Daiichi Kigenso Kagaku Kogyo, RC-100, 114 $m^2 g^{-1}$) were impregnated using an (NH_4)$_6$$H_2$$W_{12}$$O_{40}$ aqueous solution and treated using the same protocols as for WO_3/CeO_2. Samples with 10 and 15 wt% WO_3 concentrations gave BET surface areas of 101 and 93 $m^2 g^{-1}$, leading to 2.6 and 4.2 W-atom nm^{-2} surface densities, respectively.

2.2. Steady-state NO oxidation rate measurements

The reactant gases (Praxair, 3% NO/He, 1% NO_2/He, 20% O_2/He) and the He diluent (Praxair, 99.999%) were metered using electronic controllers (Porter Instruments) to give the desired reactant pressures (0.03–0.43 kPa NO, 0.01–0.23 kPa NO_2, 1–18 kPa O_2). The inlet and outlet NO and NO_2 concentrations were measured with an infrared analyzer (MKS Multi Gas Analyzer 2030, 2-cm^3 cell; 2-cm path length, 353 K).

Catalyst samples were pelleted and sieved to retain particles 125–180 μm in diameter and then diluted with quartz powder (Fluka; 125–180 μm) at quartz/catalyst mass ratios of 0.3–10 for WO_3/CeO_2 and 0–3 for CeO_2. Samples were held on a porous quartz frit within a U-shaped quartz tube (10 mm) kept at constant temperature (±0.3 K) by a resistively heated furnace. Temperatures were measured using K-type thermocouples placed at the outer reactor wall and controlled electronically (Watlow Series 96). The catalyst samples (WO_3/CeO_2; 0.035–0.9 g, CeO_2; 0.3–1.4 g, WO_3/ZrO_2; 1.4 g) were heated to 673 K at 0.08 K s^{-1} in flowing 5% O_2/He (3.3 $cm^3 s^{-1}$) and then exposed to the reactants (0.1 kPa NO, 0.05 kPa NO_2, 5 kPa O_2, 3.3 $cm^3 s^{-1}$) at 673 K for 2 h before rate measurements. The rates were measured at a standard condition (0.1 kPa NO, 0.05 kPa NO_2, 5 kPa O_2, 3.3 $cm^3 s^{-1}$) after each experiment at different conditions to ensure that changes in structure or reactivity with time did not influence the measured kinetic responses. NO_2 formation was not detected on the quartz powder used as diluent or in any transfer lines (Figs. S1 and S2 in Supplementary Information (SI)).

Intrapellet concentration or temperature gradients were ruled out by mixing WO_3/CeO_2 with fumed SiO_2 (Fluka) and then pelleting and sieving to retain 125–180 μm aggregates (intrapellet SiO_2/catalyst = 3; quartz/catalyst = 24). NO oxidation rates were unaffected by intrapellet or bed dilution (Figs. S2 and S3; SI), indicating that the local concentrations and temperatures are identical to those measured in the fluid phase; therefore, the rates reported here reflect the intrinsic chemical reaction rates devoid of transport artifacts.

2.3. Diffuse reflectance UV-visible spectroscopy

Diffuse reflectance UV-visible spectra were collected using a Cary 4 Varian spectrophotometer with a Harrick Scientific diffuse reflectance attachment (DRP-XXX) and a reaction chamber (DRA-2CR). The reaction cell was modified with a quartz frit to support catalyst samples and to improve flow and temperature uniformity. Spectra were acquired in the 1.55–6.2 eV range (0.0002–0.015 eV step, 360 s per spectrum) in 2.5–70 kPa O_2 in He, 5 kPa H_2 in He, or pure He streams. The Kubelka–Munk function [32] was used to convert reflectance (R_{sample}) into pseudo-absorbances ($F(R_\infty)$) using the reflectance of quartz powder (Fluka) as a reference white reflector ($R_{reference}$).

$$R_\infty = R_{sample}/R_{reference} \qquad (1)$$

$$F(R_\infty) = (1 - R_\infty)^2/2R_\infty \qquad (2)$$

Another operating mode was used to measure the transient responses upon addition or removal of 40 kPa O_2 from a flowing He stream (478–558 K). In this mode, the intensities were monitored at a single photon energy (3.14 eV) at 0.1 s intervals.

In situ UV-visible spectra were measured with flowing mixture (total flow rate = 3.33 cm^3 s^{-1}) of either 90% O_2/N_2 (Praxair) or H_2 (Praxair, 99.99%) with He (Praxair, 99.999%) delivered by mass flow controllers (Porter Instrument). An electrically-actuated four-way valve (Valco Instruments Company) was used for rapid switching between streams. Samples were pretreated at 623 K (0.17 K s^{-1}) in flowing 40 kPa O_2, held for 0.5 h, and then switched to He stream at 623 K for 1 h before acquiring spectra.

The reduction in these samples was monitored in flowing H_2 (373–623 K) by acquiring a spectrum in He at 50 K intervals while decreasing the temperature from 623 K to 373 K at 0.05 K s^{-1}. The He stream was replaced by a 5% H_2/He stream and spectra were collected at 50 K intervals as the temperature was increased from 373 K to 623 K (at 0.05 K s^{-1}). The weak effects of temperature on the LMCT band intensity or position were accounted for using the spectra obtained in He at the same temperatures.

3. Results and discussion

3.1. Forward NO oxidation rates on WO₃/CeO₂, CeO₂ and WO₃/ZrO₂

NO oxidation rates were measured on WO_3/CeO_2 (5.3 W nm^{-2}), CeO_2, and WO_3/ZrO_2 (4.2 W nm^{-2}). Measured NO consumption rates (r_{NO}) reflect the difference between forward ($\overrightarrow{r}_{NO}$) and reverse ($\overleftarrow{r}_{NO}$) rates for the stoichiometric NO oxidation reaction:

$$NO + 1/2 O_2 \overset{K_R}{\leftrightarrow} NO_2 \tag{3}$$

The values of $\overrightarrow{r}_{NO}$ and $\overleftarrow{r}_{NO}$ are related using the approach-to-equilibrium factor (η) [33]

$$\frac{\overleftarrow{r}_{NO}}{\overrightarrow{r}_{NO}} = \eta = \frac{[NO_2]}{K_R[NO][O_2]^{1/2}} \tag{4}$$

where K_R is the equilibrium constant for Eq. (3). Thus, the forward NO oxidation rates are obtained from Eq. (5) using the measured rates [5–8]:

$$r_{NO} = \overrightarrow{r}_{NO}(1 - \eta) \tag{5}$$

Fig. 1 shows Arrhenius plots of the forward NO oxidation rates (0.2 kPa NO, 0.055 kPa NO_2, 5 kPa O_2) on each sample normalized by their respective surface areas. These areal NO oxidation rates were about ten-fold higher on WO_3/CeO_2 than on CeO_2 and ~100-fold higher than on WO_3/ZrO_2. For transition metals and their oxides (Pt [5,6], PdO [7], RhO_2 [8] and Co_3O_4 [8] clusters), NO oxidation rates depend on their redox properties [8], leading us to infer that WO_3 domains and their interactions with CeO_2 lead to more reducible centers than those prevalent in CeO_2 surfaces (or WO_3/ZrO_2), as discussed in detail in Section 3.4.

3.2. NO, NO₂ and O₂ pressure effects on rates and elementary steps involved in NO oxidation on WO₃/CeO₂

Next, we report the effects of NO, O_2, and NO_2 pressures on forward NO oxidation rates on WO_3/CeO_2 (5.3 W nm^{-2}), determined from measured rates by accounting for approach to equilibrium ($\eta = 0.003$–0.091; Eq. (4)) at 0.03–0.37 kPa NO, 0.01–0.23 kPa NO_2, 1–18 kPa O_2, and 478–528 K. Fig. 2 shows that forward NO oxidation rates (at <10% NO conversion, per catalyst mass) increase with increasing NO and O_2 pressures, but are inhibited by NO_2 at 503 K. N_2O was not detected in the effluent stream
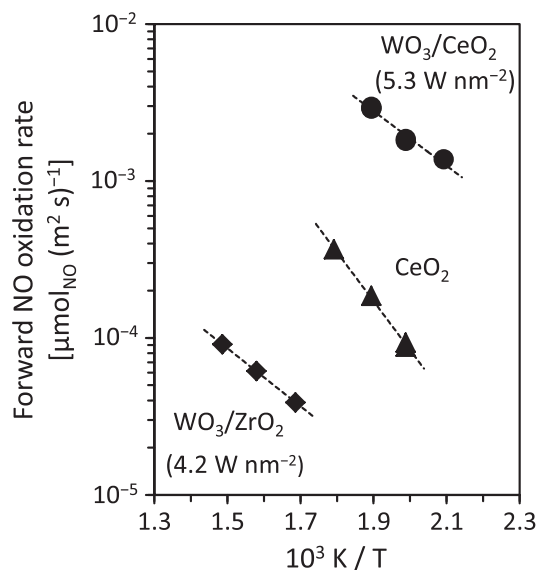

Fig. 1. Temperature dependence of the forward NO oxidation rates ($\overrightarrow{r}_{NO}$; per surface area; 0.2 kPa NO, 0.055 kPa NO_2, 5 kPa O_2) for WO_3/CeO_2 (5.3 W nm^{-2}), CeO_2, and WO_3/ZrO_2 (4.2 W nm^{-2}).

at any reaction conditions. Small axial gradients in NO_2 pressure ([NO_2]$_{out}$/[NO_2]$_{in}$ < 1.2) were taken into account by using a mean NO_2 pressure, calculated by using the observed inverse kinetic dependence of rates on NO_2 pressure [34]:

$$[NO_2]_{mean} = \frac{2}{1/[NO_2]_{in} + 1/[NO_2]_{out}} \tag{6}$$

NO oxidation rates on Pt [5,6], PdO [7], RhO_2 [8] and Co_3O_4 [8] catalysts are accurately described by the elementary steps depicted in Scheme 1, in which the kinetically-relevant step involves O_2 binding at vacancy sites (*) (step 1a) to form O_2^* on metal (Pt) or oxide (Pd, Rh, Co) surfaces nearly saturated with O^*. O^* coverages are set by quasi-equilibrated NO-NO_2 interconversions (step 1c) and O_2^* dissociates via interactions with a vicinal vacant site (step 1b). The resulting rate equation is [5–8]:

$$\overrightarrow{r}_{NO} = k_1 K_3^{-1} [NO][O_2][NO_2]^{-1} \tag{7}$$

This equation cannot accurately describe the rate data on WO_3/CeO_2 shown in Fig. 2, which exhibits sublinear effects of both NO and O_2 pressures on NO oxidation rates.

Several alternate sequences of elementary steps were examined in order to describe the kinetic effects shown in Fig. 2; these plausible schemes are shown in Section S2 in SI and they were each statistically regressed against all the rate data. These protocols led to the choice of the elementary steps shown in Scheme 2 as the most plausible sequence. This sequence leads, in turn, to a rate equation (Eq. (8), below) consistent with all rate data (dashed lines in Fig. 2).

The first step in Scheme 2 represents the reversible binding of O_2 molecules on vacant sites (*) to form O_2^* (step 2a); these molecularly adsorbed species then react with NO(g) in an irreversible step that forms NO_2 and O^* (step 2b). The direct dissociation of O_2^* via reaction with minority vacant sites (*) was also considered as alternate paths (Schemes A, B, E in Section S2; SI), but such steps cannot accurately describe the kinetic trends evident from the data in Fig. 2 and give much smaller coefficients of correlation ($R^2 = 0.859$–0.898) than the rate equation derived from the elementary steps listed in Scheme 2 ($R^2 = 0.992$). A final step (step 2c) completes a turnover via the quasi-equilibrated reactions of
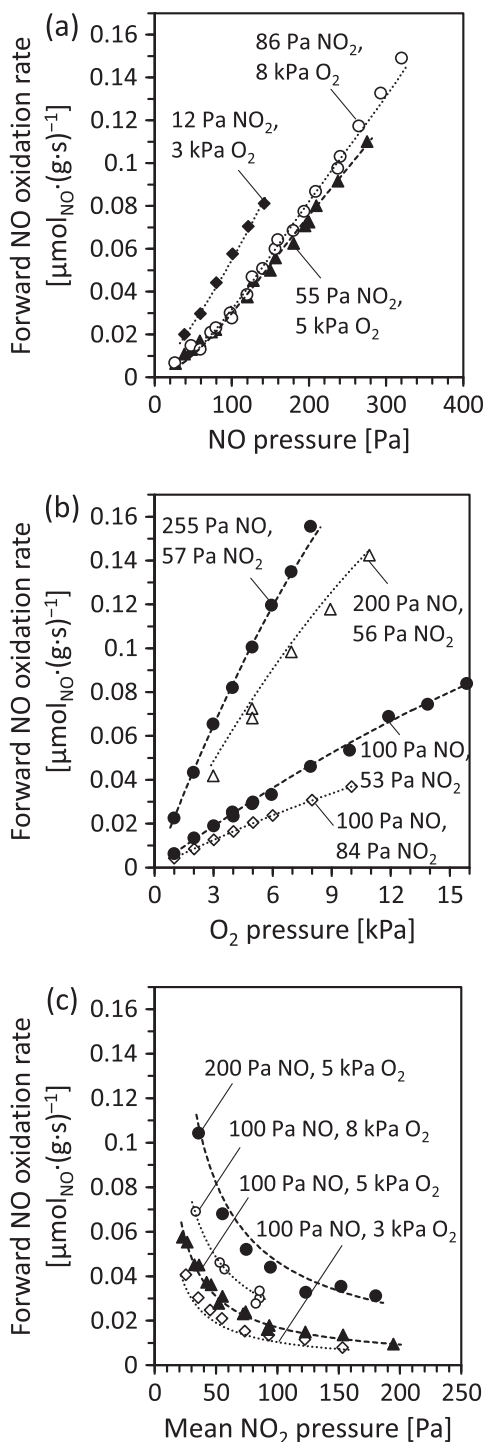
Fig. 2. Effects of NO (a), O_2 (b), and NO_2 (c) pressures on forward NO oxidation rates ($\vec{r}_{NO}$; per catalyst mass) on WO_3/CeO_2 (5.3 W nm^{-2}) at 503 K. The dashed lines denote the kinetic model predictions obtained by regressing rate data to the functional form of Eq. (8) to obtain the kinetic parameters reported in Table 1.

the second O-atom in O_2^* (O^*) with another NO molecule (as in step 1c; Scheme 1). These steps are similar to those recently suggested by DFT treatments for NO oxidation reactions on Cu/CHA, a catalytic system structurally and compositionally unrelated to the WO_3/CeO_2 catalysts examined here [16].

The steps in Scheme 2, taken together with the customary pseudo-steady-state and with the reversibility assumptions discussed above, give the rate equation (detailed derivation in Section S3; SI):
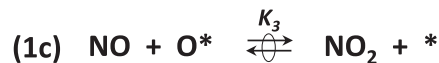
Scheme 1. Proposed elementary steps for NO oxidation reactions on Pt, PdO, RhO_2 and Co_3O_4 clusters [5–8].
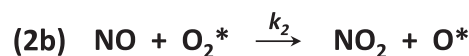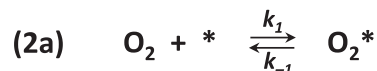
Scheme 2. Proposed elementary steps for NO oxidation on WO_3/CeO_2 and CeO_2.

$$\vec{r}_{NO} = \frac{k_1 k_2 [NO][O_2]}{k_2[NO] + k_{-1}} \cdot \frac{1}{1 + \dfrac{k_1[O_2]}{k_2[NO] + k_{-1}} + \dfrac{[NO_2]}{K_3[NO]}}$$

$$\qquad\qquad\qquad\qquad * \qquad\quad O_2^* \qquad\quad O^* \tag{8}$$

The coverages of each indicated intermediate, relative to those for vacant sites, are given by each term in the denominator of Eq. (8). The k_1 and k_{-1} terms are the forward and reverse rate constants for step 2a, k_2 is the rate constant for irreversible step 2b, and K_3 is the equilibrium constant for step 2c. The values of these rate and equilibrium constants (and their 95% confidence intervals), obtained by the regression of all rate data to the functional form of Eq. (8), are shown in Table 1.

Eq. (8) accurately describes all rate data, as evident from the parity plot of predicted and measured rates in Fig. 3. All other sequences considered with all permutations of irreversible and quasi-equilibrium steps and equilibrated NO and NO_2 adsorption on vacant sites did not account for the measured effects of reactant and product concentrations with comparable accuracy (Section S2 in SI). The sensitivity of the residuals to variations in each regressed parameter showed that all parameters in Eq. (8) could be accurately determined (Fig. S23; SI), consistent with their modest uncertainty intervals (Table 1).

Scheme 2 and Eq. (8) indicate that both steps 2a and 2b are kinetically-relevant for NO oxidation because their rate constants (k_1, k_{-1}, k_2) appear in the rate equation. The reversibility of step 2a can be determined from its approach-to-equilibrium factor (η_1):

$$\eta_1 = \frac{[O_2^*]}{[O_2][*]} \frac{k_{-1}}{k_1} = \frac{1}{(1 + k_2/k_{-1}[NO])} \tag{9}$$

The values of η_1 (from k_2 and k_{-1} values in Table 1) are 0.35–0.86 (at 478 K), 0.35–0.87 (at 503 K), and 0.34–0.86 (at 528 K) over the range of conditions used here (Section S4; SI), indicating that O_2 adsorption (step 2a) is reversible, but not quasi-equilibrated, at the conditions of these experiments.

The derivation of Eq. (8) considered O_2^*, O^* and * as relevant adsorbed species. Their (fractional) coverages ($\theta(^*)$, $\theta(O_2^*)$, $\theta(O^*)$) can be calculated from the parameters in Table 1; their ranges are 0.04–0.29, 0.03–0.24 and 0.62–0.91 for $\theta(^*)$, $\theta(O_2^*)$ and $\theta(O^*)$ at 478 K, respectively, suggesting that all species must be considered in the kinetic description of measured rates, but that O^* is

Table 1
Rate and equilibrium parameters for the NO oxidation reaction (Scheme 2) regressed using Eq. (8) and estimated energies on WO$_3$/CeO$_2$ (5.3 W nm^{-2}).

	k_1[a] [μmol_{NO} (g s Pa)$^{-1}$]	k_{-1}[a] [μmol_{NO} (g s)$^{-1}$]	k_2[a] [μmol_{NO} (g s Pa)$^{-1}$]	K_3[a] [unitless]
478 [K]	1.4 ($\pm$0.2) $\times$ 10^{-4}	4.9 ($\pm$1.2) $\times$ 10^{-1}	2.7 ($\pm$0.4) $\times$ 10^{-3}	5.5 ($\pm$1.0) $\times$ 10^{-2}
503 [K]	1.7 ($\pm$0.3) $\times$ 10^{-4}	8.0 ($\pm$2.9) $\times$ 10^{-1}	4.6 ($\pm$1.5) $\times$ 10^{-3}	6.2 ($\pm$1.2) $\times$ 10^{-2}
528 [K]	2.1 ($\pm$0.3) $\times$ 10^{-4}	1.3 ($\pm$0.5)	6.9 ($\pm$2.1) $\times$ 10^{-3}	8.6 ($\pm$ 1.7) $\times$ 10^{-2}
E_a[b] or ΔH_3[c] [kJ mol^{-1}]	16 $\pm$ 5[b]	41 $\pm$ 10[b]	40 $\pm$ 8[b]	19 $\pm$ 7[c]

[a] Obtained from regression of the kinetic data to Eq. (8) by minimization of the residuals (Section S2; SI). ($\pm$) represent 95% confidence intervals.
[b] Activation energy (E_a) to form the transition state from the reactants in each step of Scheme 2.
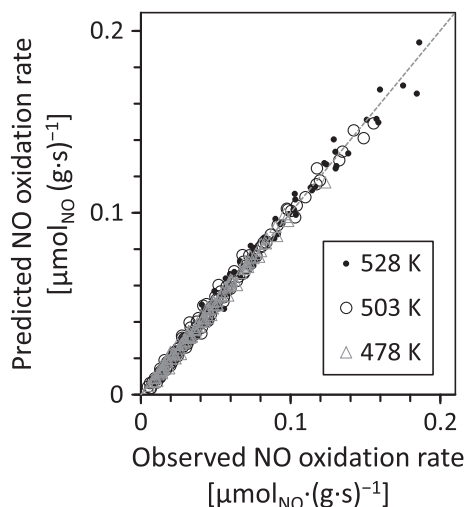[c] The enthalpy (ΔH_3) of step 2c in Scheme 2.

Fig. 3. Parity plot of measured and predicted (Eq. (8)) forward NO oxidation rates ($\vec{r}_{NO}$; per catalyst mass) on WO$_3$/CeO$_2$ (5.3 W nm^{-2}) at 478–528 K (using the kinetic and thermodynamic parameters reported in Table 1).

most abundant among these species; this is also the case at 503 K and 528 K (Section S5; SI).

Fig. 4 shows Arrhenius plots for each kinetic and thermodynamic parameter in Table 1. These data show the expected linear dependence, with slopes corresponding to activation energies or reaction enthalpy for each elementary step. The activation barrier for molecular O$_2$ adsorption transition state (16 $\pm$ 5 kJ mol^{-1}; k_1, step 2a) is smaller than that for its reverse direction (41 $\pm$ 10 kJ mol^{-1}, O$_2^*$ desorption; k_{-1}, step 2a), as expected from the exothermic nature of adsorption events. The barrier for NO-assisted O$_2^*$ dissociation (k_2, step 2b) is 40 $\pm$ 8 kJ mol^{-1}. The similar activation barriers for O$_2^*$ desorption (k_{-1}, 41 $\pm$ 10 kJ mol^{-1}) and O$_2^*$ dissociation (k_2, 40 $\pm$ 8 kJ mol^{-1}) are consistent with the reversible but not quasi-equilibrated nature of step 2a and with the kinetic relevance of both steps 2a and 2b. From the perspective of Gibbs free energies, however, the reverse step 2a would be more favorable than step 2b, because the latter, but not the former, step involves the loss of entropy upon binding of a NO(g) molecule to form the transition state for step 2b.

The reaction enthalpy for O$_2$ adsorption (ΔH_1, step 2a) is given by the difference in barriers between k_{-1} and k_1; its value is -25 ± 11 kJ mol^{-1} on WO$_3$/CeO$_2$ (5.3 W nm^{-2}), indicative of an exothermic process. Similarly, the reaction entropy (ΔS_1) for the O$_2$ adsorption step (-28 ± 24 J (K mol)$^{-1}$) is negative, as expected from the loss of degrees of freedom upon binding of a gaseous molecule onto a surface site.

The values of the reaction enthalpy for step 2c (ΔH_3) are reflected in the effects of temperature on the equilibrium constant K_3, which sets, in turn, the O* coverage during steady-state catalysis. Its value (+19 $\pm$ 7 kJ mol^{-1}) reflects the slightly endothermic

nature of step 2c in Scheme 2. Subtracting this ΔH_3 value from the enthalpy for the stoichiometric NO oxidation reaction (Eq. (3), $\Delta H_R^\circ = -57.07$ kJ mol^{-1} [35]) gives the enthalpy change (ΔH_{O^*}) for a (hypothetically) equilibrated O$_2$ adsorption step (Eq. (10)) as follows:

$$O_2 + 2* \rightleftarrows 2O^* \tag{10}$$

$$\Delta H_{O^*} = 2 \times (\Delta H_R^\circ - \Delta H_3) = -152 \pm 14 \text{ kJ mol}^{-1} \tag{11}$$

This O* adsorption enthalpy ($\Delta H_{O^*} = -152 \pm 14$ kJ mol^{-1}, Eq. (10); per mol O$_2$) is more negative than that for O$_2^*$ adsorption ($\Delta H_1 = -25 \pm 11$ kJ mol^{-1}), consistent with the prevalence of O* species during steady-state NO oxidation on WO$_3$/CeO$_2$ (at 0.62–0.91 O* ML) and with DFT-derived values for the relative enthalpies of formation of O* and O$_2^*$ on metals. For instance, these differences are 77–136 kJ mol^{-1} on CuCr$_2$O$_4$(110) [36], 97–121 kJ mol^{-1} on LaMnO$_3$(001) [37], 253 kJ mol^{-1} on ZnO(0001) [38], and 232–463 kJ mol^{-1} on RuO$_2$(110) [39].

Next, we examine WO$_3$/CeO$_2$ samples with different W surface densities (2.1–9.5 W nm^{-2}) to confirm the general nature of the mechanistic conclusions described above (Scheme 2). The effects of NO, O$_2$, and NO$_2$ pressures on NO oxidation rates, shown in Fig. 5a–c and in Figs. S25a–c (SI) for 9.5 and 2.1 W nm^{-2} samples, respectively (at 503 K), show identical trends as for the WO$_3$/CeO$_2$ sample with intermediate surface density (5.3 W nm^{-2}) (Fig. 2). The functional form of Eq. (8) accurately described all rate data (dashed lines in Figs. 5a–c and S25a–c), as shown also in Fig. 5d, leading us to conclude that the elementary steps in Scheme 2 and the resulting rate equation, are broadly applicable for all WO$_3$/CeO$_2$ samples with 2.1–9.5 W nm^{-2} surface densities.

3.3. NO, NO$_2$ and O$_2$ pressure effects on rates and elementary steps involved in NO oxidation on CeO$_2$

The effects of NO, NO$_2$ and O$_2$ pressures on (forward) NO oxidation rates were also examined on CeO$_2$ to probe any mechanistic features that may have been specifically conferred by contact with WO$_3$ domains (Fig. 6; 528 K). As for WO$_3$/CeO$_2$, the approach-to-equilibrium factors (η, Eq. (4)) for NO oxidation were much smaller than unity (0.004–0.224, 503–558 K) on CeO$_2$; measured rates were nevertheless corrected for these small thermodynamic effects to obtain forward rates (Eq. (5)). These forward rates (per mass) were more than 10-fold lower than on WO$_3$/CeO$_2$, suggesting that CeO$_2$ surfaces not in contact with WO$_3$ do not contribute to measured NO oxidation rates on WO$_3$/CeO$_2$ catalysts.

The functional form of Eq. (8) also accurately described all rate data on CeO$_2$, but the regressed parameters suggest that [*] and [O$_2^*$] coverages are much smaller than for [O*], thus leading to large uncertainties in the individual parameters and to surface coverages that could not be accurately inferred (e.g., $\theta(^*)$: 0.007–0.06; $\theta(O_2^*)$: 0.006–0.11; $\theta(O^*)$: 0.86–0.98 at 528 K; other temperatures shown in Table S3; SI). The (1 + k_1[O$_2$]/(k_2[NO] + k_{-1})) term in the denom-
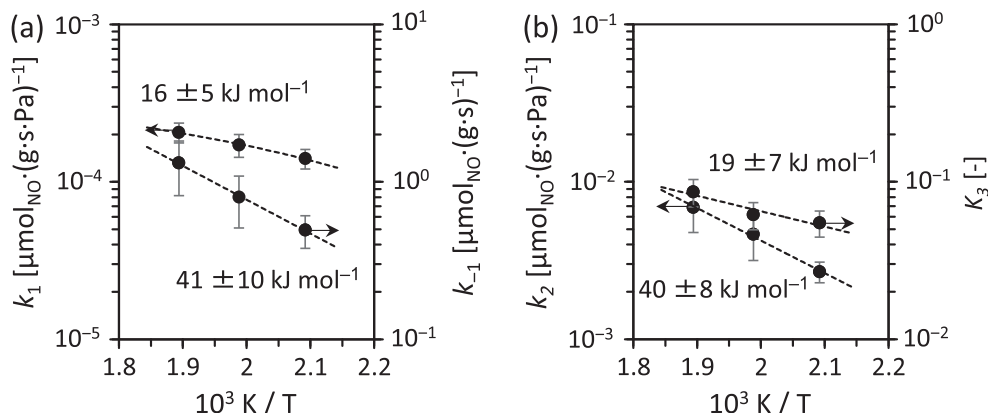
Fig. 4. Arrhenius plots of k_1 ($O_2 + * \rightarrow O_2^*$), k_{-1} ($O_2^* \rightarrow O_2 + *$), k_2 (NO + $O_2^* \rightarrow NO_2 + O^*$), and K_3 (NO + $O^* \leftrightarrow NO_2 + *$) on WO_3/CeO_2 (5.3 W nm^{-2}) regressed using Eq. (8).

inator of Eq. (8) (corresponding to [*] and [O_2^*]) is much smaller than the ([NO_2](K_3[NO])$^{-1}$) term (corresponding to [O^*]), leading to the simplified form of Eq. (12):

$$\vec{r}_{NO} = \frac{k_1 K_3 [NO]^2 [O_2]}{[NO_2]\left([NO] + \frac{k_{-1}}{k_2}\right)} \tag{12}$$

for the case when O^* as the most abundant surface intermediate (MASI) and $*$ and O_2^* are present as minority adsorbed species. This rate equation describes well all rate data on CeO_2 (dashed curves in Fig. 6). The rate and thermodynamic parameters in Eq. (12) ($k_1 K_3$ and k_{-1}/k_2) at 503–558 K are shown in Table 2; the predicted and measured rates are compared in the parity plot in Fig. 7. As for W-containing samples, the O_2 adsorption step (step 2a in Scheme 2) is reversible on CeO_2, as shown by the calculated η_1 values (0.63–0.95 at 503 K, 0.52–0.92 at 528 K, 0.39–0.85 at 558 K; details in Fig. S24; SI) and the parameters regressed from NO oxidation rates.

The Arrhenius plots for $k_1 K_3$ and k_{-1}/k_2 are shown in Fig. 8 for CeO_2 and WO_3/CeO_2 (5.3 W nm^{-2}). Apparent activation energies for $k_1 K_3$ are similar on CeO_2 (30 ± 4 kJ mol^{-1}) and WO_3/CeO_2 (35 ± 8 kJ mol^{-1}), but $k_1 K_3$ values are about 10-fold smaller on CeO_2. These data cannot discern whether such differences arise from the k_1 or K_3 terms, but it seems plausible, given the similar temperature dependences, that they merely reflect a smaller number of redox-active sites on CeO_2 than on WO_3/CeO_2, as discussed in detail in Section 3.4, where active site densities are reported based on transient UV-visible spectra and kinetic data. The temperature effects on k_{-1}/k_2 are very different on CeO_2 and WO_3/CeO_2, indicating that barriers for NO–O_2^* steps (step 2b) are larger than for O_2^* desorption (reverse step 2a) on CeO_2, but similar to each other on WO_3/CeO_2 catalysts.

3.4. In situ UV-visible absorption spectra

The experimental evidence and mechanistic conclusions in the previous sections indicate that the rates of both O_2 chemisorption to form O_2^* and of subsequent irreversible O_2^* dissociation assisted by NO influence NO oxidation turnover rates on CeO_2 and WO_3/CeO_2. Here, we probe the dynamics of O_2 binding onto vacant sites (*) from the UV-visible spectra of the relevant O_2^* intermediates upon transient changes in $O_2(g)$ concentrations at reaction temperatures. In doing so, we confirm that the parameters assigned to this specific step (k_1 and k_{-1}) indeed correspond to the purported O_2 interactions with * through comparisons of the kinetic parameters obtained from rate data and from UV-visible spectra. These data provide not only evidence for the elementary steps proposed, but also a direct and quantitative measure of the number of

redox-active sites that carry out NO oxidation turnovers. The accurate assessment of the number and the identity of such active sites in metal oxides have stood as a formidable hurdle in understanding the nature of active structures, in rigorously comparing intrinsic surface reactivities and their structural dependences, and in assessing the effects of synthesis protocols on surface properties. Here, we also use these assessments to probe the fundamental basis for the synergistic effects of WO_3 on CeO_2, which enhance the catalytic effectiveness of redox active sites at interfaces.

Fig. 9a shows UV-visible spectra for WO_3/CeO_2 (5.3 W nm^{-2}), CeO_2, and WO_3/ZrO_2 (2.6 W nm^{-2}) in contact with 0 kPa or 20 kPa O_2 at 523 K, after pretreatment in He flow at 623 K for 1.5 h. Spectral features are very similar for CeO_2 and WO_3/CeO_2 samples, leading us to assign the observed absorption band to O^{2-} ($2p$) $\rightarrow$ Ce^{4+} ($4f$) ligand-to-metal charge transfer processes in CeO_2 (LMCT [18,40]). Exposure to O_2 (20 kPa) shifts this band to lower energies for WO_3/CeO_2, but not CeO_2 or WO_3/ZrO_2, giving rise to an additional feature at ~3.2 eV (difference spectra; Fig. 9b). The absorption bands below 5 eV in WO_3/ZrO_2 are assigned to $O^{2-} \rightarrow W^{6+}$ LMCT because $O^{2-} \rightarrow Zr^{4+}$ absorption bands are expected to appear at higher energies (above 5 eV) [41–43].

Fig. 10 shows UV-visible difference spectra, obtained by subtracting the spectra after treatment in He, as a function of O_2 pressure (2.5–70 kPa) on WO_3/CeO_2 (5.3 W nm^{-2}) at 573 K. The band at 3.2 eV became more intense as the O_2 pressure increased, indicating that it arises from O_2-derived species. Similar shifts in the edge of the LMCT band have been detected on amorphous Nb_2O_5 (2.8–3.9 eV) and Ta_2O_5 (3.6–4.4 eV) upon contact with hydrogen peroxide (H_2O_2) [44] and in O_2-intercalated peroxoniobium phosphate ($NbO(O_2)_{0.5}PO_4$; 3.6 eV) prepared from $NbPO_4$ by treatment with H_2O_2 [45]. On Cu-CHA, a LMCT transition band (3.4–3.7 eV) was detected upon O_2 exposure at 673 K and assigned to the presence of an O_2 species bridged between two Cu^{2+} centers ([$Cu_2(\mu-\eta^2: \eta^2-O_2)$]$^{2+}$; [46]). Reversible O_2 binding behavior on dicopper complex [{Cu-L}$_2(\mu-\eta^2:\eta^2-O_2^{2-})$]$^{2+}$ (L: N-methyl-N,N-bis[3-(dimethylamino) propyl]-amine) was inferred from a UV-visible band at 3.4 eV assigned to side-on type peroxo species [47]. Similarly, the Ce(IV) dimer complex [Ce{N(i-Pr$_2$PO)$_2$}$_2$]$_2(\mu-\eta^2:\eta^2-O_2)_2$ in CH_2Cl_2 exhibits a band at 3.1 eV, assigned to LMCT from side-on di-μ-peroxo species to Ce [48]. Similar species with side-on type O_2 binding have been inferred from DFT calculations at Ce^{3+} centers present at CeO_2 nanoparticle surfaces ($Ce_{24}O_{47}$ and $Ce_{40}O_{79}$) [49]. The energies of these types of transitions resemble those reported here for CeO_2 and WO_3/CeO_2 catalysts (~3.2 eV; Figs. 9–11) in contact with O_2 at typical NO oxidation conditions. These previous studies [46–48] provide compelling evidence for the assignment of the bands in WO_3/CeO_2 to side-on peroxo-
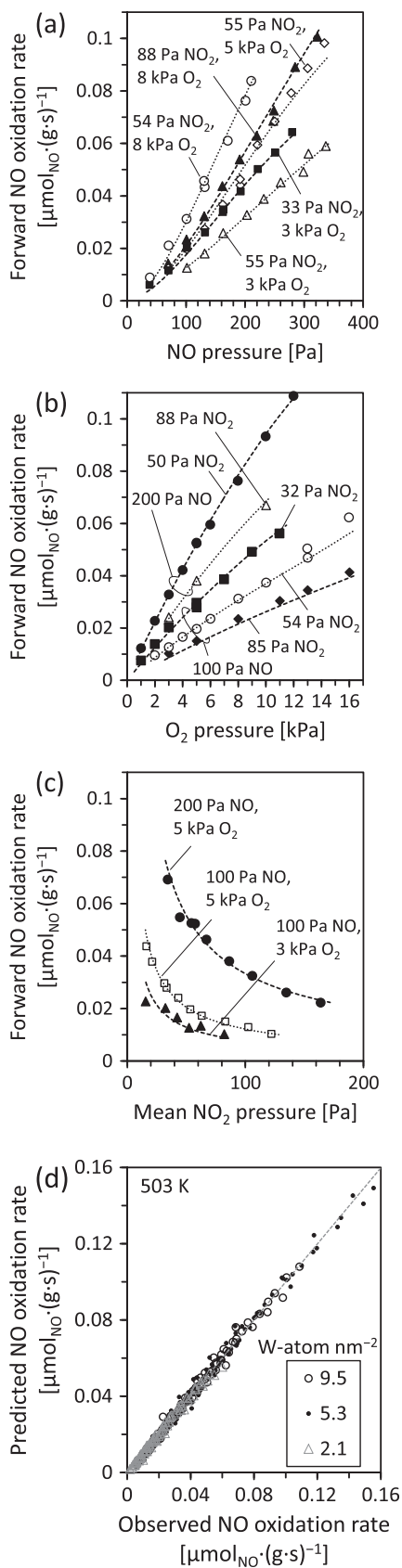
Fig. 5. Effects of the NO (a), O$_2$ (b), and NO$_2$ (c) pressures on the forward NO oxidation rates ($\overrightarrow{r}_{NO}$, per catalyst mass) on WO$_3$/CeO$_2$ (9.5 W nm^{-2}) at 503 K. The dash lines denote the fitting results using the kinetic parameters in Eq. (8); (d): parity plot for measured (2.1–9.5 W nm^{-2}, WO$_3$/CeO$_2$ at 503 K) and predicted (Eq. (8)) NO oxidation rates (using the kinetic and thermodynamic parameters reported in Tables 1 and 4).
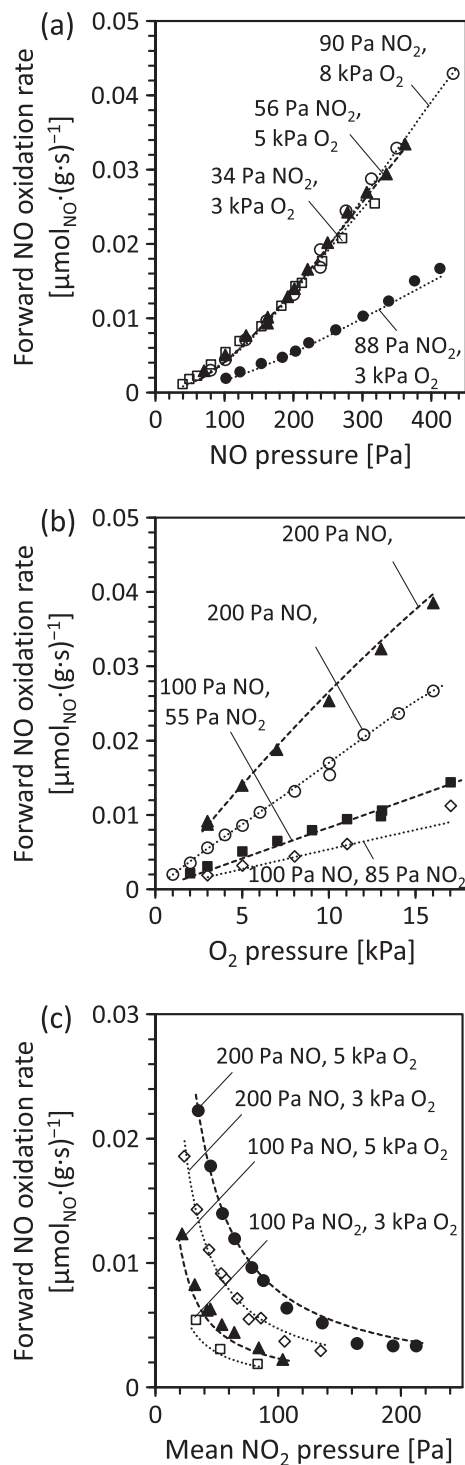

Fig. 6. Effects of NO (a), O$_2$ (b), and NO$_2$ (c) pressure on forward NO oxidation rates ($\overrightarrow{r}_{NO}$, per catalyst mass) on CeO$_2$ at 528 K. Each pressure was varied independently, while keeping the other pressures constant. Dashed curves represent rates predicted from kinetic and thermodynamic parameters (Table 2) obtained by regressing all rate data to the functional form of Eq. (12).

like O$_2^*$ species bound at vacancy sites, which are made possible, or at least more abundant, by the presence of WO$_3$ domains on CeO$_2$ surfaces (in Scheme 3).

Peroxo (O$_2^{2-}$) and superoxo (O$_2^-$) species are Raman-active and detectable in the Raman spectra of CeO$_2$ (O$_2^{2-}$; 825–890 cm^{-1} and O$_2^-$; 1125–1140 cm^{-1}, [50–52]) after prereduction with H$_2$ at 673–873 K and subsequent contact with O$_2$ (g), while these

Table 2
Rate and equilibrium parameters for NO oxidation reactions (Scheme 2) regressed using Eq. (12) on CeO_2.

Temperature [K]	$k_1 K_3$[a] [μmol (g s Pa)$^{-1}$]	k_{-1}/k_2[a] [Pa]
503	1.7 (±0.3) × 10^{-6}	7.4 (±1.8) × 10^2
528	2.5 (±0.2) × 10^{-6}	4.6 (±0.6) × 10^2
558	3.3 (±0.2) × 10^{-6}	2.2 (±0.2) × 10^2

[a] Obtained from regression of the kinetic data to Eq. (12) by minimization of residuals. (±) represent 95% confidence intervals.
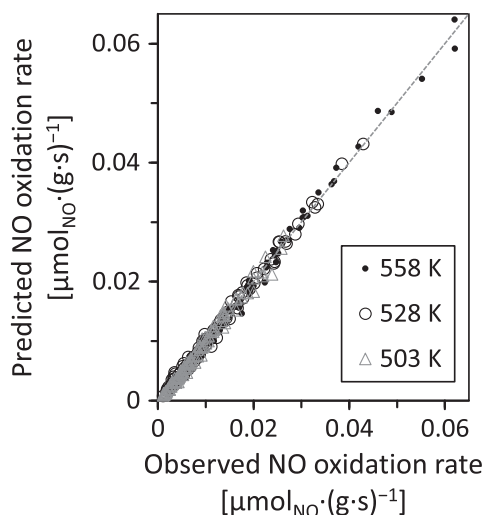

Fig. 7. Parity plot for the measured and predicted (Eq. (12)) forward NO oxidation rates ($\vec{r}_{NO}$, per catalyst mass) on CeO_2 at 503−558 K with the kinetic parameters shown in Table 2.

features are absent on samples pretreated with He before exposure to $O_2(g)$. The He treatment at 623 K in our experiments did not create the reduced centers required to form peroxo (or superoxo) species upon subsequent contact with $O_2(g)$, thus precluding the formation and spectroscopic detection of these latter species on CeO_2 after He treatment (Fig. 9). In contrast, WO_3 domains on CeO_2 allow the formation of reduced Ce centers in He (at 623 K) near their interfaces via W−O−Ce interaction (Scheme 3; discussed in detail in Section 3.6), leading to UV-visible features for O_2^* species upon contact with $O_2(g)$; these findings are consistent with the fact that [*], [O_2^*] and [O*] species are prevalent on WO_3/ CeO_2 (Eq. (8)), but only [O*] species are dominating on CeO_2 (Eq. (12)) surfaces, a conclusion independently reached from their respective NO oxidation rate equations (Sections 3.2 and 3.3).

The effect of H_2 treatment at 373–623 K on the number of reduced Ce^{3+} and W^{5+} centers formed was probed using UV-visible spectroscopy on WO_3/CeO_2 (5.3 W nm^{-2}), CeO_2, WO_3/ZrO_2 (2.6 W nm^{-2}), and monoclinic bulk WO_3 powders (Sigma–Aldrich, 99.9%). Fig. 11 shows difference spectra in H_2 (5 kPa) after subtraction of the respective spectra in He. The negative features at ∼3.2 eV, evident in WO_3/CeO_2 after H_2 treatment above 473 K, correspond to the disappearance of the same spectral features that emerged upon exposing these samples to $O_2(g)$ at 523 K and 573 K (Figs. 9b and 10). These negative features became more intense with increasing H_2 treatment temperatures (473–623 K). These trends were also observed on CeO_2 (but only when treated in H_2 above 623 K) and the band on CeO_2 was nearly coincident with that on WO_3/CeO_2 (inset in Fig. 11), suggesting that they arise from similar O_2^* species. We conclude that WO_3 domains increase the rate of formation of reduced centers in CeO_2; such reduced centers in CeO_2 are evident from the Raman band (at ∼550 cm^{-1}) [51] that emerges upon reduction in H_2 of CeO_2 above 773 K.

Neither WO_3/ZrO_2 nor monoclinic WO_3 samples showed negative features at ∼3.2 eV upon contact with H_2 at 373–623 K; instead, such treatments led to new features below 2.5 eV, which were particularly intense on bulk WO_3. These features arise from d-d transitions in W^{5+} centers, caused by either the formation of $H^{\delta+}$ species or by the removal of H_2O to form O-vacancies [43]. Such W^{6+} reduction processes become more facile as domains become larger, because of more effective electron delocalization upon reduction [43], consistent with the appearance of such features at 473 K on large WO_3 crystallites, but only at higher temperatures (∼623 K) on the smaller domains prevalent in WO_3/ZrO_2 (Fig. 11). On WO_3/CeO_2, these reduced centers became detectable at lower temperatures (473 K) than in WO_3/ZrO_2 (623 K), in part, because of the higher W density in WO_3/CeO_2 (5.3 W nm^{-2}) than in WO_3/ZrO_2 (2.6 W nm^{-2}) samples. These differences in reducibility also reflect the more reducible nature of the CeO_2 support relative to ZrO_2, consistent with the coincident emergence of more intense d-d transitions in W^{5+} centers (<2.5 eV) and with the observed decrease in the intensity of the LMCT bands in CeO_2 (3.2 eV) upon exposure of WO_3/CeO_2 to H_2 at increasing temperatures from 423 to 623 K (the correlation between the d-d transition and LMCT bands is shown in Fig. S26; SI).

These data provide evidence for intimate electronic contact between WO_x domains and CeO_2 surfaces. Similar synergistic effects have been reported for CuO domains on CeO_2, for which the reduction of CuO and the formation of vacancies in CeO_2 are enhanced by their intimate contact [53]. Similar support effects have been reported on WO_3 catalysts, for which supports with smaller band gaps (e.g., SnO_2 and ZrO_2) gave more reducible WO_x domains than those with larger band gaps (e.g., SiO_2 and Al_2O_3)
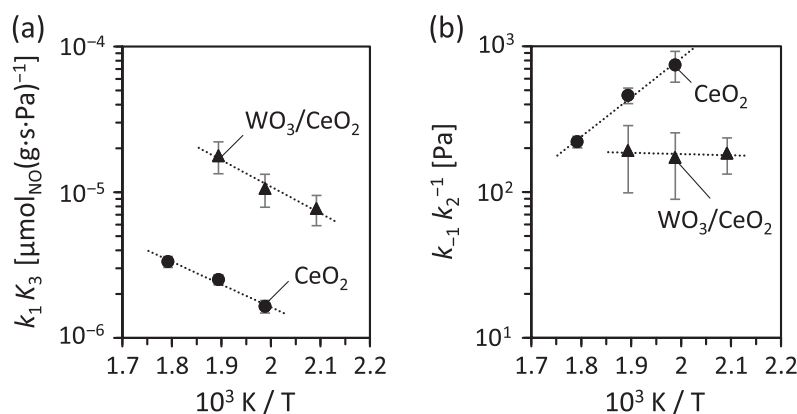

Fig. 8. Arrhenius plots of the kinetic parameters of $k_1 K_3$ (a) and $k_{-1} k_2^{-1}$ (b) regressed using Eq. (12) on CeO_2 and using Eq. (8) on WO_3/CeO_2 (5.3 W nm^{-2}).
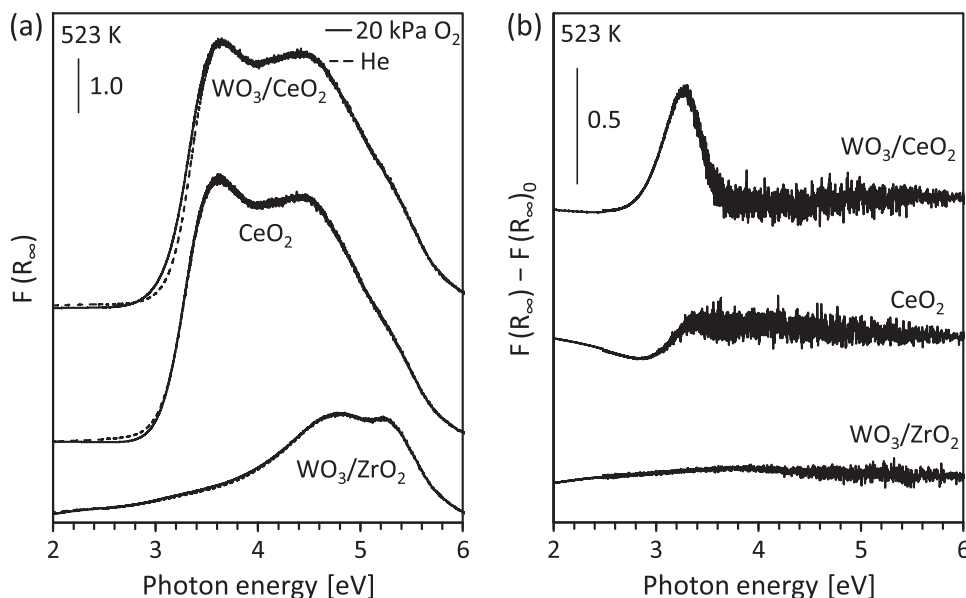
Fig. 9. *In situ* UV-visible spectra in He and in 20 kPa O_2 (a) and UV-visible difference spectra in 20 kPa O_2 (b) on WO_3/CeO_2 (5.3 W nm^{-2}), CeO_2, and WO_3/ZrO_2 (2.6 W nm^{-2}) at 523 K after pretreatment in He at 623 K for 1.5 h. The difference spectra (b) are obtained by subtracting from each spectra in (a); the spectra for the respective samples after He treatment (F(R$_\infty$)$_0$) and the introduction of O_2 (F(R$_\infty$)).
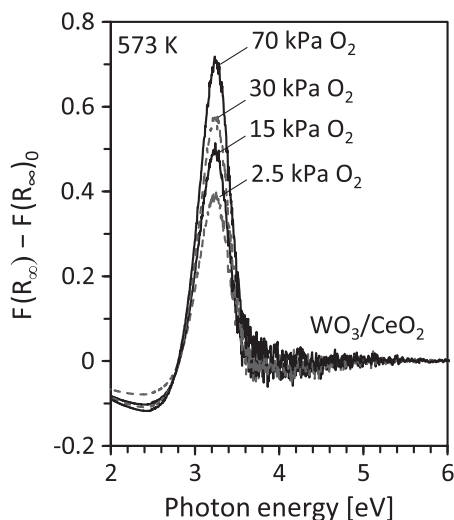

Fig. 10. UV-visible difference spectra in 2.5–20 kPa O_2 (by subtraction of spectrum in He; F(R$_\infty$)$_0$) on WO_3/CeO_2 (5.3 W nm^{-2}) at 573 K after treatment in flowing He at 623 K for 1.5 h.

because of more effective electronic isolation of WO_x on the more insulating oxide supports [54].

3.5. Transient response of UV-visible spectra to changes in the reduction-oxidation potential of contacting gases

The dynamics of the reversible adsorption of O_2 on WO_3/CeO_2 (5.3 W nm^{-2}) were monitored by monitoring transient changes in their UV-visible spectra upon changes in O_2 concentrations in the contacting gaseous phase (3.14 eV band; 503 K, 558 K) after treatment in He at 623 K for 1.5 h (Fig. 12a). Exposure to O_2 (at 0.1 ks) from He led to sharp increase in absorbance, which then remained essentially constant with time (denoted A_{eq}); subsequent exposure to He (at 1.3 ks) returned the band to its initial intensity (denoted A_0) at 558 K. Similar reversible changes were observed at 503 K, suggesting that sintering or irreversible structural changes did not occur upon O_2 cycling and that these spectral changes were

caused by reversible O_2 adsorption-desorption processes (step 2a in Scheme 2). These transient responses (Fig. 12a) showed an initial fast process (~20 s) after O_2 pressure perturbations and a much slower subsequent response (~2000 s) as shown in a logarithmic scale for the data obtained at 558 K (Fig. 12b). The initial fast response coincides with catalytic rate transients observed upon changing reactant concentrations; these data indicate, in contrast to the subsequent slow transients, that such initial rapid LMCT processes are associated with the formation and desorption of kinetically-relevant O_2-derived species on CeO_2 surfaces interacting with WO_3 domains.

Fig. 12c shows the intensity (in a logarithmic scale) in the fast transient region after a switch from He to O_2 (40 kPa) and then from O_2 to He at 558 K. The slopes of the resulting linear trends are larger for O_2 adsorption (He → O_2 ($A_{eq} - A_{t1}$)) than for O_2^* desorption (O_2 → He ($A_{t2} - A_0$)) cycles, consistent with the kinetic results inferred from NO oxidation rate analysis ($k_1[O_2]_{40kPa}/k_{-1}$ values of 11.4 and 6.3 at 478 K and 528 K; Table 3). The band intensities shown in Fig. 12c are proportional to O_2^* coverages and the evolution of these O_2^* species with time reflects the net rates of O_2 adsorption and O_2^* desorption elementary steps:

$$\frac{d[O_2^*]}{dt} = k_1[O_2][*] - k_{-1}[O_2^*] \tag{13}$$

Integrating Eq. (13) (detailed derivations in Section S8; SI) then gives the following:

$$\frac{(A_{eq} - A_{t1})}{(A_{eq} - A_0)} = e^{-(k_1[O_2]+k_{-1})t} \tag{14}$$

$$\frac{(A_{t2} - A_0)}{(A_{eq} - A_0)} = e^{-k_{-1}t} \tag{15}$$

where A_{t1} is the absorbance during contact with 40 kPa O_2 at any time t_1 and A_{t2} is absorbance during contact with He at any time t_2 (Fig. 12a). The rate parameters (k_1 and k_{-1}) are obtained by linear regression of UV-visible transient data in Fig. 12c; their values are listed in Table 3 (at 478 K, 503 K, 528 K and 558 K). The ratio of the O_2 adsorption to the O_2^* desorption rate constants (k_1/k_{-1}) from transient UV-visible data is shown in Fig. 13, where their similarity
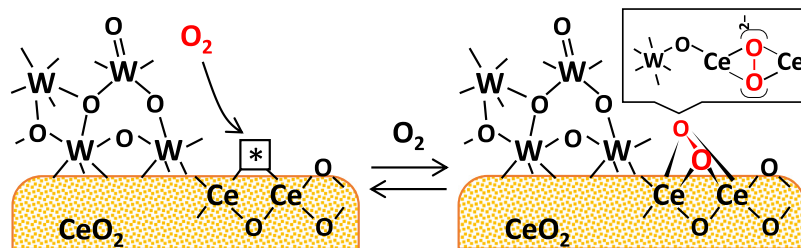
Scheme 3. Schematic depiction of plausible O_2 binding modes on vacancies at CeO_2 surfaces induced by interactions with WO_3 domains.

with those derived independently from the kinetic analysis of NO oxidation rates is evident (Section 3.2). These similar ratios confirm that the O_2^* species detected by its LMCT band in the presence of $O_2(g)$ correspond to those formed via the kinetically-relevant O_2 adsorption step (step 2a) in Scheme 2 in reactions of NO-O_2 mixtures.

The individual rate constants for O_2 adsorption and desorption steps derived from the UV-visible transient ($k_1^{UV vis}$ and $k_{-1}^{UV vis}$) reflect the intrinsic reactivity of each redox-active site, while those derived from kinetic data ($k_1^{ss kin}$ and $k_{-1}^{ss kin}$) are values normalized by the catalyst mass of each sample, by convention but also because of the absence of a more rigorous choice. The ratios of these two rate constants, each derived from independent measurements represent the areal density of redox-active sites (ρ_1 and ρ_{-1}):

$$\rho_1 = \frac{k_1^{ss kin}}{k_1^{UV vis}} \cdot \frac{N_A}{S_m} \tag{16}$$

$$\rho_{-1} = \frac{k_{-1}^{ss kin}}{k_{-1}^{UV vis}} \cdot \frac{N_A}{S_m} \tag{17}$$

where N_A is Avogadro's constant [atoms mol^{-1}] and S_m is surface area [m^2 mol^{-1}]. The values of ρ_1 and ρ_{-1} (shown in Table 3 and Fig. 13) are similar to each other and nearly independent of temperature (478–528 K). These data indicate that the number of surface species able to undergo redox cycles is not strongly influenced by temperature.

3.6. Effects of the WO_3 content on redox-active site densities and NO oxidation turnover rates

The density of redox-active sites on 2.1 and 9.5 W nm^{-2} WO_3/CeO_2 was also examined using the protocols specifically described for the 5.3 W nm^{-2} WO_3/CeO_2 sample in the previous section. Such protocols cannot be applied to pure CeO_2, because spectral features for O_2-derived species are too weak for transient analysis (Fig. 9). The regressed parameters measured on WO_3/CeO_2 are shown in Table 4 at 503 K. The k_{-1} and k_2 values from NO oxidation rates on the 2.1 W nm^{-2} sample are less certain than for the 5.3 W nm^{-2} and 9.5 W nm^{-2} samples, because of detectable contributions from those parts of CeO_2 surfaces not in contact with WO_3 domains. The left axis in Fig. 14a shows redox-active site densities (ρ_1 and ρ_{-1}) obtained by comparing the rate constants determined from kinetic and UV-visible spectral data for each WO_3/CeO_2 sample. These areal active site densities increased as W densities increased from 2.1 to 9.5 W nm^{-2}, albeit with some greater uncertainties in the measurements on the 2.1 W nm^{-2} sample.

The number and type of redox-active sites, seldom accessible to rigorous inquiry on heterogeneous catalysts and especially on metal oxides, are required to express reactivity as turnover rates. In this case, the areal active site densities (ρ_1 and ρ_{-1}) allow us to measure such intrinsic reactivities as NO oxidation turnover rates (0.1 kPa NO, 0.05 kPa NO$_2$, 5 kPa O$_2$, 503 K) shown in Fig. 14a (right axis). These turnover rates appear to be independent of W surface density within experimental uncertainties.

These turnover rates allow direct comparisons of reactivity with those reported previously on Pt [6], PdO [7], and RhO$_2$ [8] catalysts (0.12 kPa NO, 0.056 kPa NO$_2$, 5 kPa O$_2$; 603 K; Fig. 14b), on which the elementary steps include kinetically-relevant O_2 activation on vacancies at surfaces nearly saturated with O^* adatoms (step 1a; Scheme 1). Turnover rates on 2.1–9.5 W nm^{-2} WO_3/CeO_2 samples were extrapolated to 603 K by using measured activation energies (Table 1) and the same reactant compositions (0.12 kPa NO, 0.056 kPa NO$_2$, 5 kPa O$_2$) using Eq. (8). Turnover rates on WO_3/ CeO_2 were lower than on noble metals, except for the case of small PdO (<2.0 nm) clusters (Fig. 14b), but provide competitive rates at lower temperatures because activation energies are lower on WO_3/ CeO_2 than on noble metals. The apparent activation energies on these noble metals are consistent with a small activation barrier
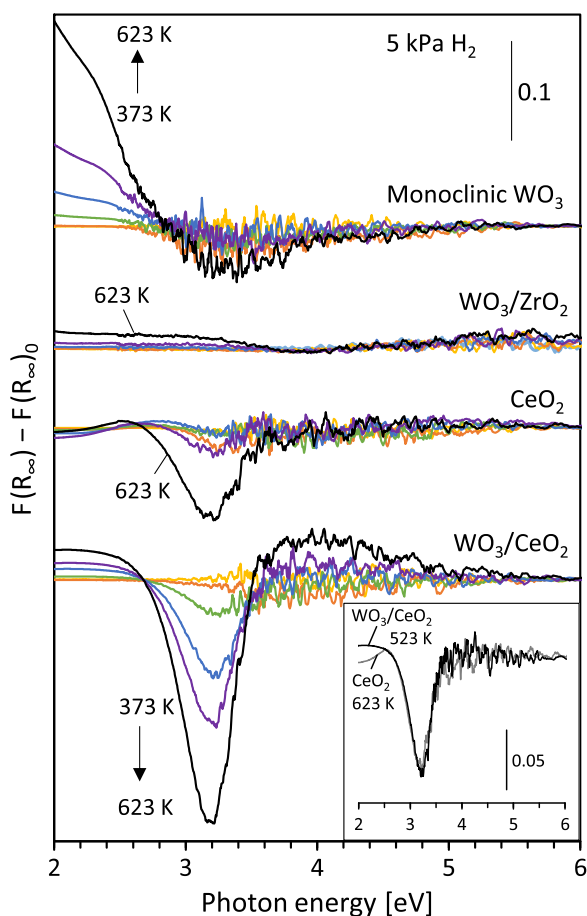

Fig. 11. UV-visible difference spectra in 5 kPa H$_2$ at 373–623 K at 50 K intervals subtracted by the spectrum in He ($F(R_\infty)_0$) at the same temperature on WO_3/CeO_2 (5.3 W nm^{-2}), CeO_2, WO_3/ZrO_2 (2.6 W nm^{-2}), and monoclinic WO_3 after pretreatment in He at 623 K for 1.5 h. Inset: Comparison of the spectra on WO_3/CeO_2 (523 K) and CeO_2 (623 K).
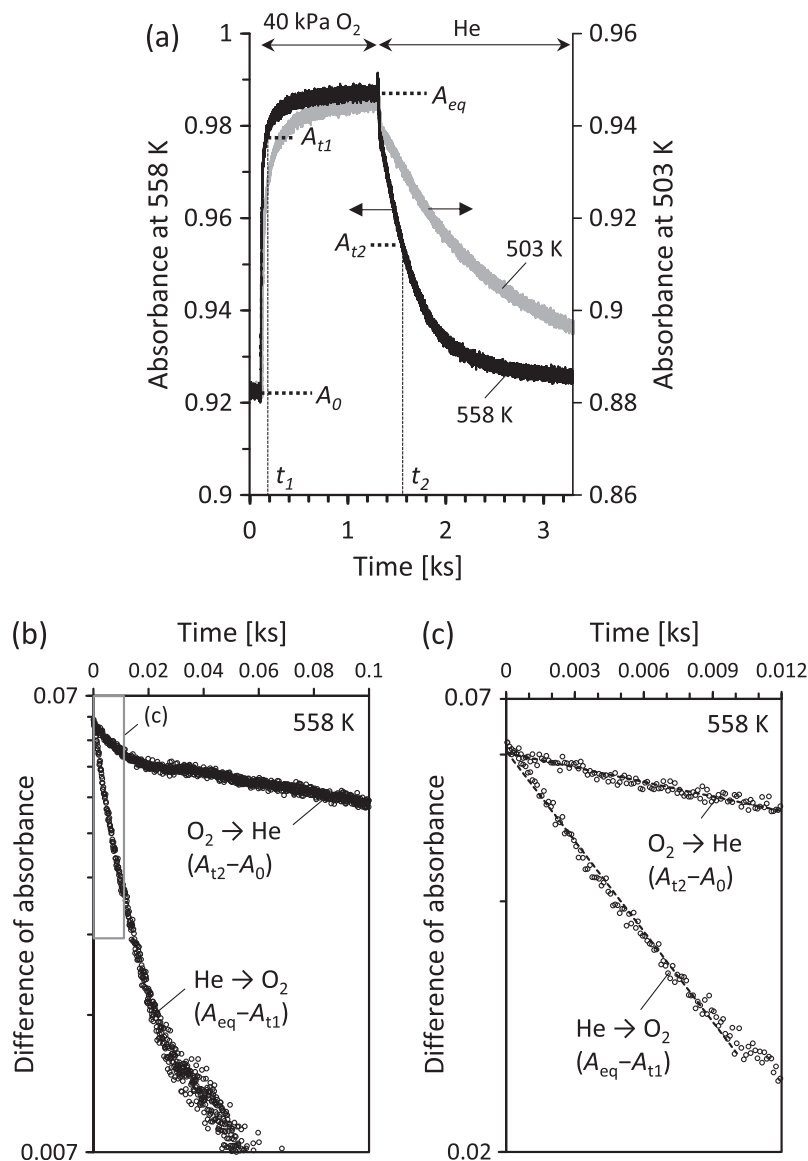
Fig. 12. Transient changes in absorbance bands at 3.14 eV in linear ((a); 503 K and 558 K) and logarithmic ((b), (c); 558 K) scales after switching from He to O_2 (40 kPa) and from O_2 to He on WO_3/CeO_2 (5.3 W nm^{-2}) treated in He at 623 K for 1.5 h. (A_0; initial absorbance in He after the pretreatment, A_{eq}; equilibrium absorbance in 40 kPa O_2, A_{t1}; absorbance during O_2 adsorption in 40 kPa O_2 at any time t_1, A_{t2}; absorbance during O_2 desorption in He at any time t_2).

Table 3
Rate constants (k_1 and k_{-1}) and the density of redox-active site (ρ_1 and ρ_{-1}) determined from transient UV-visible responses (478–558 K) on WO_3/CeO_2 (5.3 W nm^{-2}).

Temperature [K]	478	503	528	558
$k_1^{UV\,vis\,a}$ [10^3 (ks Pa)$^{-1}$]	1.26 (±0.01)	1.22 (±0.02)	1.37 (±0.02)	1.59 (±0.02)
$k_{-1}^{UV\,vis\,a}$ [ks^{-1}]	3.7 (±0.2)	6.0 (±0.2)	8.5 (±0.2)	12.2 (±0.3)
ρ_1^b [atom nm^{-2}]	1.7 (±0.2)	2.2 (±0.4)	2.3 (±0.3)	–[d]
ρ_{-1}^c [atom nm^{-2}]	2.1 (±0.5)	2.1 (±0.7)	2.4 (±0.9)	–[d]

[a] From linear regression of transient UV-visible responses (up to 0.01–0.015 ks) using Eqs. (14) and (15).
[b] From k_1 from NO oxidation rate analysis and transient UV-visible response using Eq. (16).
[c] From k_{-1} from NO oxidation rate analysis and transient UV-visible response using Eq. (17).
[d] NO oxidation rates were not measured at 558 K.

for O_2 reaction with $*$ and a very exothermic O_2 dissociation step to form O^*, giving measured activation energies of 82 ± 9 kJ mol^{-1} (2.4 nm Pt; [5]) and 125 ± 4 kJ mol^{-1} (2.0 nm Pt; [6]) on Pt/Al$_2$O$_3$.

The apparent activation energies on 5.3 W nm^{-2} WO_3/CeO_2 are much smaller (32 ± 2 kJ mol^{-1}; 0.1 kPa NO, 0.05 kPa NO$_2$, 5 kPa O$_2$), leading to a much weaker dependence on temperature, thus allowing these catalysts to remain active as temperatures decrease to those relevant for diesel exhaust treatment. Indeed, the measured turnover rates on 5.3 W nm^{-2} WO_3/CeO_2 at 503 K (0.22 ± 0.04 × 10^{-3} s^{-1}; 0.1 kPa NO, 0.05 kPa NO$_2$, 5 kPa O$_2$) are similar to those on Pt (0.22 ± 0.07 × 10^{-3} s^{-1} [5]; 0.026 ± 0.004 × 10^{-3} s^{-1} [6]), when the latter are extrapolated using reported activation energies [5,6]. These WO_3/CeO_2 catalysts become significantly more active than those based on noble metals when rates are compared based on catalyst mass (or volume), the relevant basis for such comparisons in their practical use. For examples, forward NO oxidation rates on 5.3 W nm^{-2} WO_3/CeO_2 at 503 K (2.96 ± 0.20 × 10^{-8} mol$_{NO}$ (g s)$^{-1}$) are ~20–40 times higher than reported on more costly Pt-based catalysts (0.14 ± 0.04 × 10^{-8} mol$_{NO}$ (g s)$^{-1}$ [5]; 0.07 ± 0.01 × 10^{-8} mol$_{NO}$ (g s)$^{-1}$ [6]).
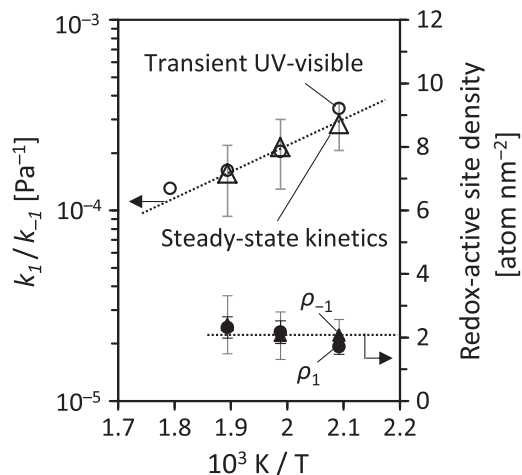
Fig. 13. Temperature dependence of k_1/k_{-1} from transient UV-visible analyses (○; Table 3) and from steady-state NO oxidation rate analyses (Δ; Table 1), and of the redox active site density from ρ_1 (●; Eq. (16)) and ρ_{-1} (▲; Eq. (17)) on WO$_3$/CeO$_2$ (5.3 W nm^{-2}).

The turnover rates on these transition metal and oxide clusters depend on their mean cluster size (Fig. 14b), because the removal of oxygen atoms from oxides and from metal surfaces becomes more facile with increasing cluster size; this reflects a concomitant decrease in their HOMO-LUMO gaps [55,56], thus allowing the placement of electrons at a lower-lying LUMO during these reductive events. The resulting higher steady-state density of vacancies, as a result of the more reducible centers, is thus responsible for the higher turnover rates observed on larger clusters during NO oxidation redox cycles [6–8]. The thermodynamics of such vacancy formation on clusters rigorously depend on redox thermodynamics, as shown by the relation between NO oxidation turnover rates on Pt, PdO, RhO$_2$, Co$_3$O$_4$ and their reduction potentials as aqueous cations (Pt^{2+}/Pt^0, Pd^{2+}/Pd^0, Rh^{4+}/Rh^{3+}, Co^{3+}/Co^{2+}) [8,57].

On WO$_3$/CeO$_2$, vacancies in CeO$_2$ form preferentially at WO$_3$-–CeO$_2$ interfaces (Scheme 3), which emerge during synthesis through interactions between aqueous polytungstate oligomers and CeO$_2$, plausibly by forming Ce-containing heteropolytungstate intact or lacunary clusters through mechanisms denoted as "ligand-promoted oxide dissolution" [58,59]. These processes have been shown to lead to the formation of AlW$_{10-12}$
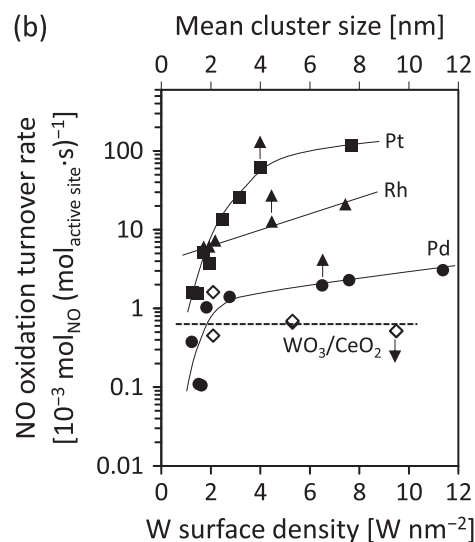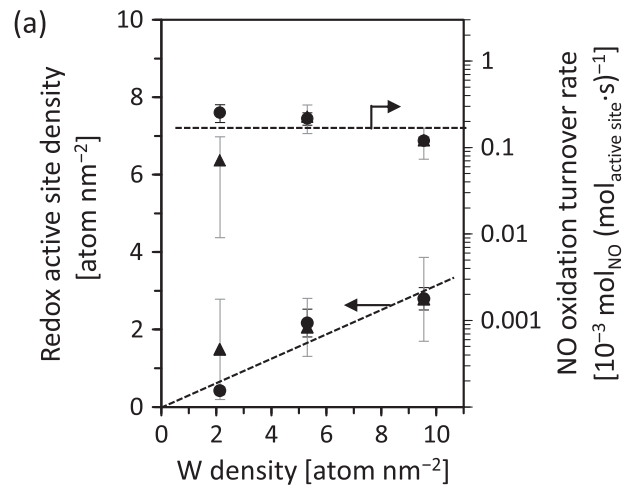

Fig. 14. (a) Redox-active site density (from Eqs. (16) and (17)) and NO oxidation turnover rates (0.1 kPa NO, 0.05 kPa NO$_2$, 5 kPa O$_2$, 503 K) normalized by active site density from ρ_1 (●; Eq. (16)) and ρ_{-1} (▲; Eq. (17)) on WO$_3$/CeO$_2$. (b) NO oxidation turnover rate (0.12 kPa NO, 0.056 kPa NO$_2$, 5 kPa O$_2$; 603 K) on Pt/Al$_2$O$_3$ (■) [6], RhO$_2$/Al$_2$O$_3$ (▲) [7], PdO/Al$_2$O$_3$ (●) [8] and WO$_3$/CeO$_2$ (◇; 2.1, 5.3 and 9.5 W nm^{-2} (this study) estimated from extrapolation of the Arrhenius dependence (Fig. 4) of the rate parameters in Eq. (8)).

Table 4
Rate constants (k_1, k_{-1}, k_2 and K_3) and the density of redox-active site (ρ_1 and ρ_{-1}) determined from NO oxidation rate measurement (503 K) and transient UV-visible responses (503 K) on WO$_3$/CeO$_2$ (2.1–9.5 W nm^{-2}).

W surface density	Measurement	k_1	k_{-1}	k_2 [μmol$_{NO}$ (g s Pa)$^{-1}$]	K_3 [unitless]	ρ_1[g] [atom nm^{-2}]	ρ_{-1}[h] [atom nm^{-2}]
2.1 [W nm^{-2}]	NO oxidation rate data[a]	7.5 (±1.2) × 10^{-5}[c]	3.3 ± 2.8[e]	5.8 (±4.8) × 10^{-3}	1.0 (±0.2) × 10^{-1}	0.4 ± 0.1	1.5 ± 1.3
	Transient UV-visible[b]	2.2 (±0.1) × 10^{-3}[d]	27 ± 1[f]	–	–		
5.3 [W nm^{-2}]	NO oxidation rate data[a]	1.7 (±0.3) × 10^{-4}[c]	8.0 (±2.9) × 10^{-1}[e]	4.6 (±1.5) × 10^{-3}	6.2 (±1.2) × 10^{-2}	2.2 ± 0.4	2.1 ± 0.7
	Transient UV-visible[b]	12.2 (±0.02) × 10^{-4}[d]	6.0 ± 0.2[f]	–	–		
9.5 [W nm^{-2}]	NO oxidation rate data[a]	1.0 (±0.1) × 10^{-4}[c]	9.5 (±3.4) × 10^{-1}[e]	3.3 (±0.9) × 10^{-3}	1.0 (±0.2) × 10^{-1}	2.8 ± 0.3	2.8 ± 1.1
	Transient UV-visible[b]	6.1 (±0.1) × 10^{-4}[d]	5.8 ± 0.9[f]	–	–		

[a] From regression of the kinetic data to Eq. (8) by minimization of residuals.
[b] From linear regression of transient UV-visible responses using Eqs. (14) and (15).
[c] [μmol$_{NO}$ (g s Pa)$^{-1}$] units.
[d] [(ks Pa)$^{-1}$] units.
[e] [μmol$_{NO}$ (g s)$^{-1}$] units.
[f] [ks^{-1}] units.
[g] From k_1 values determined from NO oxidation rates and transient UV-visible data using Eq. (16).
[h] From k_{-1} values determined from NO oxidation rates and transient UV-visible data using Eq. (17).

[58] and SiW_{12} [60] structures during contact of Al_2O_3 and SiO_2 with solvated $(NH_4)_{10}H_2W_{12}O_{42}$ species. Mo-based heteropolyoxometalate (POM) clusters have also been detected upon contact of Al_2O_3 [59] and SiO_2 [61] with solvated hepta-molybdate $(NH_4)_6Mo_7O_{24}$ and hexamolybdate $(n-Bu_4N)_2Mo_6O_{19}$ precursors, respectively. The size and high coordination number of Ce cations would preclude their placement as tetrahedral central atoms in Keggin structures; they have been reported, however, to form linkages among anionic polytungstates (W_5-W_{148}) with $Ce^{3+/4+}$ cations [62–65]. Solvated Ce cations can react with terminal O-atoms in POM $(PW_{12}O_{40}^{3-})$ clusters dispersed on mesoporous silica (MCM-41), leading to the formation of Ce—O—W bonds [66], as may also happen with Ce ions at CeO_2 surfaces during the synthesis of the WO_3/CeO_2 materials in the present study.

CeO_2 species in contact with WO_3 domains are more reducible than on pure CeO_2 as expected from the LMCT band shifts in CeO_2 after H_2 treatment at 373–623 K (Fig. 11). The number of Ce^{3+} species formed at ultra-high vacuum conditions and detected in the X-ray photoelectron spectrum of WO_3/CeO_2 [67,68] increased with increasing WO_3 content [67], indicating that the formation of O-vacancies is promoted by WO_3 domains. DFT-derived Ce—O bond lengths increase near a W-atom placed on CeO_2 (1 1 1) surfaces, consistent with a weakening of the Ce—O bonds [69]. Theoretical treatments also indicate that O-atom vacancies preferentially form at interfaces between CeO_2 and ZrO_2 crystallites [70], as a result of lattice distortions that also lengthen Ce—O bonds and lead to more stable reduced Ce^{3+} centers [71].

These previous studies provide confirmatory evidence for the mechanistic interpretations provided here for the enhancement of NO oxidation turnovers by promotion of CeO_2 with WO_3 domains and for nature and location of the redox-active centers. A more direct assessment of the reactive properties of these WO_3-CeO_2 interfaces requires more precise structural models of such interfaces and theoretical descriptions of their electronic properties and of the geometry and energy of intermediates and transition states that mediate O_2^* activation steps (step 2a; Scheme 2). The current study provides the underpinnings and the mechanistic guidance for such theoretical treatments and for the emergence of more accurate guidance for designing catalytic surfaces with even greater reactivity in NO oxidation catalysis and also in other CeO_2-catalyzed oxidation reactions mediated by O_2 dissociation steps [72].

4. Conclusions

Rate equations derived from rigorous kinetic measurements of NO oxidation on WO_3/CeO_2 and CeO_2 are consistent with a mechanism describing two kinetically-relevant steps: reversible non-dissociative O_2 chemisorption, and subsequent NO assisted, irreversible O_2^* dissociation, which is in sharp contrast to the prevalent mechanism involving an unassisted O_2 dissociation as kinetically-relevant step on other transition metal catalysts [5–8]. Reversible shifts of the $O_{2p} \rightarrow Ce_{4f}$ LMCT bands ($\sim$3.2 eV) in the UV-visible spectra on WO_3/CeO_2 in response to O_2 addition and removal (478–558 K) are attributed to the formation of O_2^* intermediates, while no such shifts are detected on CeO_2, suggesting changes in the redox properties of CeO_2 surfaces through interaction with WO_3 domains. The O_2 binding dynamics onto vacant sites (*) monitored by UV-visible spectra allow for the determination of rate constants corresponding to O_2 adsorption on and desorption from redox-active sites. The number of such active sites, seldom experimentally accessible in redox reactions on oxides, is measured by combining mechanistic interpretation of NO oxidation rate data

with transient UV-visible responses. The density of these redox-active sites increases with increasing W surface density (2.1–9.5 W nm^{-2}), although NO oxidation turnover rates (per active site) are essentially independent of the WO_3 surface density. Hence, we infer that atomic contact between WO_3 domains and CeO_2 induces the formation of these redox-active sites near their interface and that the identity of WO_3-CeO_2 interaction remains essentially unchanged with W surface density measured here. While the observed turnover rates (per site) are similar to those on Pt-based catalysts at typical temperatures for diesel exhaust ($\sim$500 K), rates based on catalyst mass are >10-fold higher, rendering WO_3/CeO_2 of practical interest as SCR components as well as in diesel oxidation catalysts. These findings and quantitative interpretations not only provide a clear mechanistic picture of the dynamics of NO oxidation reactions on WO_3/CeO_2, but also conceptual insights into the genesis of redox-active sites and the activation of peroxo intermediates via bimolecular pathways.

Appendix A. Supplementary material

Supplementary data associated with this article can be found, in the online version, at http://dx.doi.org/10.1016/j.jcat.2016.07.011.

References

[1] W.A. Glasson, C.S. Tuesday, J. Am. Chem. Soc. 85 (1963) 2901–2904.
[2] P.S. Monks, Chem. Soc. Rev. 34 (2005) 376–395.
[3] G. Busca, L. Lietti, G. Ramis, F. Berti, Appl. Catal. B: Environ. 18 (1998) 1–36.
[4] M. Wallin, C.-J. Karlsson, M. Skoglundh, A. Palmqvist, J. Catal. 218 (2003) 354–364.
[5] S.S. Mulla, N. Chen, W.N. Delgass, W.S. Epling, F.H. Ribeiro, Catal. Lett. 100 (2005) 267–270.
[6] B.M. Weiss, E. Iglesia, J. Phys. Chem. C 113 (2009) 13331–13340.
[7] B.M. Weiss, E. Iglesia, J. Catal. 272 (2010) 74–81.
[8] B.M. Weiss, N. Artioli, E. Iglesia, ChemCatChem 4 (2012) 1397–1404.
[9] M.M. Yung, E.M. Holmgreen, U.S. Ozkan, J. Catal. 247 (2007) 356–367.
[10] E. Park, S. Chin, J. Jeong, J. Jurng, Micropor. Mesopor. Mater. 163 (2012) 96–101.
[11] M. Casapu, O. Kröcher, M. Mehring, M. Nachtegaal, C. Borca, M. Harfouche, D. Grolimund, J. Phys. Chem. C 114 (2010) 9791–9801.
[12] I. Lezcano-Gonzalez, U. Deka, H.E. van der Bij, P. Paalanen, B. Arstad, B.M. Weckhuysen, A.M. Beale, Appl. Catal. B: Environ. 154–155 (2014) 339–349.
[13] D.W. Fickel, E. D'Addio, J.A. Lauterbach, R.F. Lobo, Appl. Catal. B: Environ. 102 (2011) 441–448.
[14] J.H. Kwak, D. Tran, S.D. Burton, J. Szanyi, J.H. Lee, C.H.F. Peden, J. Catal. 287 (2012) 203–209.
[15] S.J. Schmieg, S.H. Oh, C.H. Kim, D.B. Brown, J.H. Lee, C.H.F. Peden, D.H. Kim, Catal. Today 184 (2012) 252–261.
[16] A.A. Verma, S.A. Bates, T. Anggara, C. Paolucci, A.A. Parekh, K. Kamasamudram, A. Yezerets, J.T. Miller, W.N. Delgass, W.F. Schneider, F.H. Ribeiro, J. Catal. 312 (2014) 179–190.
[17] W. Shan, F. Liu, H. He, X. Shi, C. Zhang, Chem. Commun. 47 (2011) 8046–8048.
[18] Z. Ma, D. Weng, X. Wu, Z. Si, J. Environ. Sci. 24 (2012) 1305–1316.
[19] Y. Peng, K. Li, J. Li, Appl. Catal. B: Environ. 140–141 (2013) 483–492.
[20] L. Chen, J. Li, M. Ge, Environ. Sci. Technol. 44 (2010) 9590–9596.
[21] L. Chen, J. Li, M. Ge, R. Zhu, Catal. Today 153 (2010) 77–83.
[22] Y. Li, H. Cheng, D. Li, Y. Qin, Y. Xie, S. Wang, Chem. Commun. (2008) 1470–1472.
[23] F. Can, S. Berland, S. Royer, X. Courtois, D. Duprez, ACS Catal. 3 (2013) 1120–1132.

[24] M. Casapu, A. Bernhard, D. Peitz, M. Mehring, M. Elsener, O. Kröcher, Appl. Catal. B: Environ. 103 (2011) 79–84.
[25] R. Qu, X. Gao, K. Cen, J. Li, Appl. Catal. B: Environ. 142–143 (2013) 290–297.
[26] Z. Ma, D. Weng, X. Wu, Z. Si, B. Wang, Catal. Commun. 27 (2012) 97–100.
[27] N.-Y. Topsøe, Science 265 (1994) 1217–1219.
[28] R.Q. Long, R.T. Yang, J. Catal. 194 (2000) 80–90.
[29] M. Devadas, O. Kröcher, M. Elsener, A. Wokaun, G. Mitrikas, N. Söger, M. Pfeifer, Y. Demel, L. Mussmann, Catal. Today 119 (2007) 137–144.
[30] X. Gao, Y. Jiang, Y. Zhong, Z. Luo, K. Cen, J. Hazard. Mater. 174 (2010) 734–739.
[31] M. Iwasaki, K. Dohmae, Y. Nagai, T. Tanaka, Unpublished results.
[32] P. Kubelka, F. Munk, Z. Tech. Phys. 12 (1931) 593–601.
[33] W.L. Holstein, M. Boudart, J. Phys. Chem. B 101 (1997) 9991–9994.
[34] M. García-Diéguez, E. Iglesia, J. Catal. 301 (2013) 198–209.
[35] R.L. David, Handbook of Chemistry and Physics, 87th ed., CRC Press, Boca Raton, FL, 2006.
[36] X.-L. Xu, W.-K. Chen, J.-Q. Li, J. Mol. Struct. (Thoechem) 860 (2008) 18–23.
[37] E.A. Kotomin, Y.A. Mastrikov, E. Heifets, J. Maier, Phys. Chem. Chem. Phys. 10 (2008) 4644–4649.
[38] J. Sołtys, J. Piechota, M. Łopuszyński, S. Krukowski, J. Cryst. Growth 374 (2013) 53–59.
[39] Y.D. Kim, A.P. Seitsonen, S. Wendt, J. Wang, C. Fan, K. Jacobi, H. Over, G. Ertl, J. Phys. Chem. B 105 (2001) 3752–3758.
[40] A. Migani, G.N. Vayssilov, S.T. Bromley, F. Illas, K.M. Neyman, Chem. Commun. 46 (2010) 5936–5938.
[41] M. Scheithauer, R.K. Grasselli, H. Knözinger, Langmuir 14 (1998) 3019–3029.
[42] A. Gutiérrez-Alejandre, J. Ramírez, G. Busca, Catal. Lett. 56 (1998) 29–33.
[43] D.G. Barton, M. Shtein, R.D. Wilson, S.L. Soled, E. Iglesia, J. Phys. Chem. B 103 (1999) 630–640.
[44] M. Ziolek, I. Sobczak, P. Decyk, L. Wolski, Catal. Commun. 37 (2013) 85–91.
[45] L. Moreno-Real, E.R. Losilla, M.A.G. Aranda, M. Martínez-Lara, S. Bruque, M. Gabás, J. Solid State Chem. 137 (1998) 289–294.
[46] F. Giordanino, P.N.R. Vennestrom, L.F. Lundegaard, F.N. Stappen, S. Mossin, P. Beato, S. Bordiga, C. Lamberti, Dalton Trans. 42 (2013) 12741–12761.
[47] Ga.Y. Park, M.F. Qayyum, J. Woertink, K.O. Hodgson, B. Hedman, A.A.N. Sarjeant, E.I. Solomon, K.D. Karlin, J. Am. Chem. Soc. 134 (2012) 8513–8524.
[48] G.C. Wang, H.H.Y. Sung, I.D. Williams, W.H. Leung, Inorg. Chem. 51 (2012) 3640.
[49] G. Preda, A. Migani, K.M. Neyman, S.T. Bromley, F. Illas, G. Pacchioni, J. Phys. Chem. C 115 (2011) 5817.
[50] M. Daniel, S. Loridant, J. Raman Spectrosc. 43 (2012) 1312–1319.
[51] Z. Wu, M. Li, J. Howe, H.M. Meyer, S.H. Overbury, Langmuir 26 (2010) 16595–16606.
[52] Y.M. Choi, H. Abernathy, H.-T. Chen, M.C. Lin, M. Liu, ChemPhysChem 7 (2006) 1957–1963.
[53] Y. Nagai, K. Dohmae, Y.F. Nishimura, H. Kato, H. Hirata, N. Takahashi, Phys. Chem. Chem. Phys. 15 (2013) 8461–8465.
[54] J. Macht, C.D. Baertsch, M. May-Lozano, S.L. Soled, Y. Wang, E. Iglesia, J. Catal. 227 (2004) 479–491.
[55] L.E. Brus, J. Chem. Phys. 80 (1984) 4403–4409.
[56] Y. Wang, N. Herron, J. Phys. Chem. 95 (1991) 525–532.
[57] Y.-H. Chin, M. Garcia-Dieguez, E. Iglesia, J. Phys. Chem. C 120 (2016) 1446–1460.
[58] X. Carrier, J.B. Caillerie, J.F. Lambert, M. Che, J. Am. Chem. Soc. 121 (1999) 3377–3381.
[59] X. Carrier, J.F. Lambert, M. Che, J. Am. Chem. Soc. 119 (1997) 10137–10146.
[60] C. Martín, P. Malet, G. Solana, V. Rives, J. Phys. Chem. B 102 (1998) 2759–2768.
[61] C.R. Deltcheff, M. Amirouche, M. Che, J.M. Tatibouët, M. Fournier, J. Catal. 125 (1990) 292–310.
[62] B.S. Bassil, U. Kortz, Z. Anorg. Allg. Chem. 636 (2010) 2222–2231.
[63] W. Chen, X. Wang, Y. Jiao, P. Huang, E. Zhou, Z. Su, K. Shao, Inorg. Chem. 53 (2014) 9486–9497.
[64] J. Iijima, E. Ishikawa, Y. Nakamura, H. Naruke, Inorg. Chim. Acta 363 (2010) 1500–1506.
[65] K. Suzuki, F. Tang, Y. Kikukawa, K. Yamaguchi, N. Mizuno, Angew. Chem. Int. Ed. 53 (2014) 5356–5360.
[66] T. Takashima, R. Nakamura, K. Hashimoto, J. Phys. Chem. 113 (2009) 17247–17253.
[67] L. Chen, J. Li, W. Ablikim, J. Wang, H. Chang, L. Ma, J. Xu, M. Ge, H. Arandiyan, Catal. Lett. 141 (2011) 1859–1864.
[68] C. Liu, L. Chen, H. Chang, L. Ma, Y. Peng, H. Arandiyan, J. Li, Catal. Commun. 40 (2013) 145–148.
[69] A. Joshi, A. Rammohan, Y. Jiang, S. Ogunwumi, J. Mol. Struct. (Thoechem) 912 (2009) 73–81.
[70] D.S. Aidhy, B. Liu, Y. Zhang, W.J. Weber, J. Phys. Chem. C 118 (2014) 30139–30144.
[71] D. Ma, Z. Lu, Y. Tang, T. Li, Z. Tang, Z. Yang, Phys. Lett. A 378 (2014) 2570–2575.
[72] F. Yang, J. Graciani, J. Evans, P. Liu, J. Hrbek, J.F. Sanz, J.A. Rodriguez, J. Am. Chem. Soc. 133 (2011) 3444–3451.